JOURNAL OF SYNCHROTRON RADIATION

ISSN 1600-5775

Received 2 March 2019
Accepted 23 April 2019

Edited by M. Weik, Institut de Biologie Structurale, France

Keywords: metalloprotein; enzyme; radiation damage; specific structural damage; xylose isomerase; dose; structural pertubation.

PDB references: xylose isomerase, 6qrr; 6qrs; 6qrt; 6qru; 6qrv; 6qrw; 6qrx; 6qry

Supporting information: this article has supporting information at journals.iucr.org/s

Structural knowledge or X-ray damage? A case study on xylose isomerase illustrating both

Helena Taberman,[a,b] Charles S. Bury,[b] Mark J. van der Woerd,[c] Edward H. Snell[d,e]* and Elspeth F. Garman[b]*

[a]Macromolecular Crystallography (HZB-MX), Helmholtz-Zentrum Berlin, Albert-Einstein Straße 15, 12489 Berlin, Germany, [b]Department of Biochemistry, University of Oxford, South Parks Road, Oxford OX1 3QU, UK, [c]Department of Enterprise Technology Services, 2001 Capitol Avenue, Cheyenne, WY 82001, USA, [d]Hauptman-Woodward Medical Research Institute, 700 Ellicott Street, Buffalo, NY 14203, USA, and [e]Materials Design and Innovation, State University of New York at Buffalo, 700 Ellicott Street, Buffalo, NY 14203, USA.
*Correspondence e-mail: esnell@hwi.buffalo.edu, elspeth.garman@bioch.ox.ac.uk

Xylose isomerase (XI) is an industrially important metalloprotein studied for decades. Its reaction mechanism has been postulated to involve movement of the catalytic metal cofactor to several different conformations. Here, a dose-dependent approach was used to investigate the radiation damage effects on XI and their potential influence on the reaction mechanism interpreted from the X-ray derived structures. Radiation damage is still one of the major challenges for X-ray diffraction experiments and causes both global and site-specific damage. In this study, consecutive high-resolution data sets from a single XI crystal from the same wedge were collected at 100 K and the progression of radiation damage was tracked over increasing dose (0.13–3.88 MGy). The catalytic metal and its surrounding amino acid environment experience a build-up of free radicals, and the results show radiation-damage-induced structural perturbations ranging from an absolute metal positional shift to specific residue motions in the active site. The apparent metal movement is an artefact of global damage and the resulting unit-cell expansion, but residue motion appears to be driven by the dose. Understanding and identifying radiation-induced damage is an important factor in accurately interpreting the biological conclusions being drawn.

1. Introduction

During the process of X-ray diffraction, the crystals used in the experiment also absorb X-ray radiation, causing primary damage and also generating free radicals, which propagate chemical damage through radiation chemistry pathways (Nave, 1995; O'Neill *et al.*, 2002). This is an inherent problem in macromolecular crystallography (MX) even when the samples are held at cryogenic temperatures (~100 K) (Holton, 2009; Garman, 2010). These radicals cause structural perturbations that result in both global and site-specific effects. Global effects can be observed during data collection, for example as a loss of diffraction intensity, increased Wilson *B*-factors, and swelling of the unit-cell volume causing increasing non-isomorphism (Ravelli & McSweeney, 2000). In contrast, specific effects can often be seen in electron density maps after refinement. These can occur at less than 60 times lower dose before any signs of radiation damage are observed on the diffraction images or are seen from the decreasing data quality (Holton, 2009). Site-specific damage can be detected, for example in the photoreduction of metal centres, as elongation and breakage of disulfide bonds, and decarboxylation of acidic side chains (Ravelli & McSweeney, 2000; Carugo &

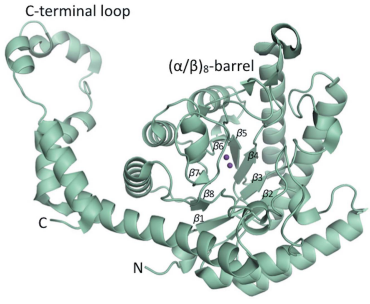

Carugo, 2005; Weik *et al.*, 2000; Burmeister, 2000). These can distort the biological conclusions drawn from the resultant model (Grabolle *et al.*, 2006) and the various radiation damage effects can also hinder efficient structure solution.

The metal centres of metalloproteins, which constitute 25–50% of all proteins found within an organism (Bowman *et al.*, 2016), have a very large X-ray absorption cross-section (Murray & Garman, 2002) and are highly electron-affinic (Williams, 1985), increasing the probability that the radiation and its subsequent secondary products will affect them. Hence, the metal ion and its surrounding amino acid environment experience a localized build-up of free radicals, which makes them more susceptible to damage than the rest of the protein. This causes, for example, changes in the redox state of the metal sites, which can compromise the active site structure and again have an effect on the biological conclusions being drawn (Corbett *et al.*, 2007).

The 43 kDa metalloprotein xylose isomerase (XI; EC 5.3.1.5), also referred to as glucose isomerase, holds enormous potential for applications in the pharmaceutical industry and in biotechnology for converting biomass into fuels and chemicals. It is an important enzyme used extensively in the food industry in large-scale production of starch-based high-fructose corn syrup (Bhosale *et al.*, 1996; Pedersen, 1993). XI catalyses the reversible isomerization of a broad range of aldose sugars to their corresponding ketoses using two divalent metal cofactors (designated M1 and M2), such as Mg^{2+}, Mn^{2+} or Co^{2+} (Carrell *et al.*, 1984; Callens *et al.*, 1986; Jokela *et al.*, 2002), of which XI has the highest affinity for manganese ($K_d = 2.7 \times 10^{-5}$ *M*) (Schray & Mildvan, 1972). It is thus of great interest to understand the reaction mechanism and thereby potentially increase its suitability for different industrial processes, for example by improving its activity, specificity, thermal stability and optimum pH.

The exact reaction mechanism of XI has long been a subject of debate fed by increasingly detailed studies, many discussing the mobility of the catalytic metal ion (M2) (Collyer *et al.*, 1990; Jenkins *et al.*, 1992; Allen *et al.*, 1994; Lavie *et al.*, 1994; Whitaker *et al.*, 1995; Asbóth & Náray-Szabó, 2000; Fenn *et al.*, 2004; Lee *et al.*, 2017). The overall mechanism is thought to include three major steps: ring opening, isomerization and ring closure. The binding of the cyclic α-anomer carbohydrate substrate, including the role of the stabilizing structural metal (M1), is well defined (Asbóth & Náray-Szabó, 2000; Blow *et al.*, 1992). However, the subsequent steps in the reaction mechanism, during which the catalytic metal ion M2 is said to adopt as many as three different alternate positions, M2*a*, M2*b* and M2*c*, remain unclear. Fig. 1 shows a schematic representation of the reaction mechanism and putative role of the alternate M2 positions. Recent X-ray and neutron diffraction studies have established that the ring opening and linearization proceeds through a proton transfer reaction in which the doubly protonated His54 in the active site acts as a proton donor and Lys289 as a proton acceptor, and presumably M2 moves from position M2*a* to position M2*b* to bind the linear substrate (Fenn *et al.*, 2004; Kovalevsky *et al.*, 2010; Munshi *et al.*, 2014). The subsequent isomerization step then occurs through hydride shift from a catalytic water mediated by the essential M2 cofactor, position M2*c* (Lavie *et al.*, 1994; Whitaker *et al.*, 1995; Fenn *et al.*, 2004; Kovalevsky *et al.*, 2010; Whitlow *et al.*, 1991), after which the bonds to M2 are lost. The acyclic product is then stabilized by a ring closure reaction (Bhosale *et al.*, 1996).

Currently, there are 156 structural models of XI, determined by X-ray or neutron diffraction, or by a combination of both, deposited in the Protein Data Bank (Berman *et al.*, 2000). There is no consensus between the structures regarding the conformation(s) of M2 or its importance and role in the reaction mechanism. In general, neutron diffraction experiments, although limited by the neutron fluxes available, complement X-ray diffraction by being more sensitive to the visualization of hydrogen atoms (or their deuterium isotopes) in structures, which leads to more detailed definitions of enzymatic reaction mechanisms. Unfortunately, the neutron scattering cross-section of some metal atoms, for example Mg and Mn, is small and they scatter neutrons more weakly than X-rays. Furthermore, the neutron scattering length of the Mg (5.375 fm) or Mn (3.73 fm) atoms is similar to that of a single D (6.61 fm) or H (3.74 fm) atom, making it challenging to distinguish the metals explicitly from water molecules in mobile regions of a protein. Hence, X-ray diffraction studies of metalloproteins are crucial to provide structural and mechanistic detail, even though metal atoms and their immediate environment are highly sensitive to X-ray radiation damage.

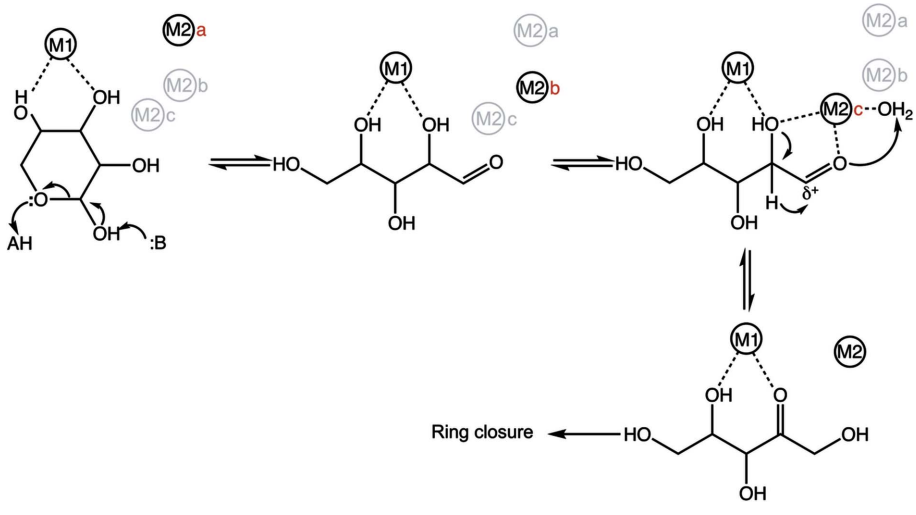

Figure 1
Schematic presentation of the reaction mechanism of XI converting xylose to xylulose with the putative mobility of the catalytic metal ion with conformations M2*a*, M2*b* and M2*c*. Mechanism based on Asbóth & Náray-Szabó (2000), Fenn *et al.* (2004) and Munshi *et al.* (2014).

In this study, we report the effects of dose-dependent radiation damage on XI and examine its impact, if any, on identifying the precise reaction mechanism. Fenn *et al.* (2004) review evidence suggesting mobility of the catalytic metal cofactor, M2. Given the radiation sensitivity of metal sites, we explore this possibility in light of the dose-dependent effects we observe. The results highlight the need to be aware of the radiation damage inflicted during structural studies of metalloproteins, and to understand how global and specific effects may impact the interpretations from resulting models.

2. Materials and methods

2.1. Protein purification and crystallization

The enzyme used in this study was the thermostable E186Q mutant of *Streptomyces rubiginosus* XI previously supplied by Genencor International (Palo Alto, California, USA) and routinely used in most XI studies. The protein was purified as described previously (Meilleur *et al.*, 2006; Snell *et al.*, 2006). Briefly, the commercial XI was purified with gel-filtration chromatography using a HiLoad 16/600 Superdex 200 column and finally dialysed in 50 m*M* magnesium sulfate. The purified enzyme was stored at 22°C as a dilute solution (∼3 mg ml^{-1}) and concentrated to 100 mg ml^{-1} immediately before setting up the crystallization experiments.

The protein was transported to Stanford Synchrotron Radiation Lightsource (SSRL, Stanford, USA) where crystals were grown at the synchrotron by the hanging drop vapour diffusion crystallization method. Concentrated protein (5 µl at 100 mg ml^{-1}) was mixed with an equal volume of reservoir solution and equilibrated against 1 ml of precipitant solution. The successful crystallization conditions were 8% (*v*/*v*) 2-propanol, 25% (*v*/*v*) ethylene glycol, 50 m*M* HEPES pH 7.0 and 50 m*M* magnesium chloride. Orthorhombic crystals grew in less than a day at room temperature (22°C) to dimensions of 0.3 mm × 0.3 mm × 0.3 mm. Inclusion of additional cryo-protectant was not necessary, since the ethylene glycol concentration was sufficient to avoid any ice formation on cooling, and, after harvesting with nylon cryo-loops, the crystals were flash-cooled to 100 K directly into the nitrogen cryostream for data collection using an Oxford Instruments CryojetXL (Oxford Instruments, Abingdon, UK).

2.2. Diffraction data collection, processing, structure solution and refinement

X-ray diffraction data were collected at SSRL on beamline 11-1 using an ADSC Quantum 315 CCD detector. Seven consecutive data sets were collected from the same crystal, each starting at the same orientation and position as the first to ensure that the same volume of the crystal was irradiated during each data set. A complete data set was first collected to 1.21 Å resolution (largest inscribed circle on detector) at an X-ray energy of 13.0 keV (0.954 Å wavelength) over 90° of rotation, with a crystal-to-detector distance of 150 mm, 0.5° oscillation angle and 2 s exposure time per image. An identical 10° high-resolution swathe was collected up to 0.89 Å resolution (largest inscribed circle) between each complete data set on the first 10° of the complete 90° wedge at an X-ray energy of 14.5 keV (wavelength of 0.855 Å) with a crystal-to-detector distance of 100 mm. A 0.5° oscillation angle and 35 s exposure time per image was used to monitor the decay of the high-resolution (HR) reflections and to increase the absorbed X-ray dose between the seven complete data sets. While the expected intensity decay was visually observed in the high-resolution swathes, the completeness was approximately 17%, and thus our study focuses only on the complete 90° data sets and the structural models obtained from them. All data sets were processed with *XDS* (Kabsch, 2010), which was also used to generate a random 5% $R_{\rm free}$ test set of the unmerged reflections for the first low-dose data set.

The 0.86 Å resolution structure of XI from *Streptomyces olivochromogenes* (PDB code: 1muw) (Fenn *et al.*, 2002), which has 95% sequence identity with the *S. rubiginosus* XI E186Q mutant, was used as a starting model. The lowest-dose data set was used with this starting model in *ARP/wARP* (Perrakis *et al.*, 1999; Langer *et al.*, 2008) to produce a new starting model minimizing any phase bias. The structure was initially refined with this starting model using *REFMAC5* (Murshudov *et al.*, 2011) followed by *phenix.refine* (Afonine *et al.*, 2012) from the *PHENIX* software suite (Adams *et al.*, 2010) and finalized with *SHELXL* (Sheldrick, 2015). The `.pdb` file from phenix.refine was converted into a `.ins` file with *PDB2INS* (Lübben & Sheldrick, 2019). The occupancy and anisotropic *B*-factors of all atoms were refined.

In between the refinement steps, manual rebuilding of the model took place using *COOT* (Emsley *et al.*, 2010). The *hkl* data file used for the *SHELXL* refinement was converted to a `.mtz` file with *FREERFLAG* from the CCP4 program suite (Winn *et al.*, 2011) and the existing $R_{\rm free}$ test set was retained. The same test set was also copied to the higher-dose data sets when scaling them with *AIMLESS* (Evans, 2006, 2011; Evans & Murshudov, 2013) and truncating them all to 1.17 Å resolution. For each of the six subsequent higher-dose data sets and the overall summed data set (all seven data sets merged), individual structures were derived using *phenix.refine* with the structure obtained above for the first (low-dose) data set coupled with the observed amplitudes of each later data set. The structures were validated with the *MolProbity* (Chen *et al.*, 2010) and other structure validation tools within *phenix.refine* and *COOT*, and using *PDB_REDO* (Joosten *et al.*, 2014) and the wwPDB Validation Server (Berman *et al.*, 2003). The processing and refinement statistics for each data set are summarized in Table 1. The atomic coordinates and the structure factors for the resulting eight structures have been deposited in the wwPDB (Berman *et al.*, 2003; Gutmanas *et al.*, 2014).

2.3. Dose calculation

RADDOSE-3D (Zeldin *et al.*, 2013*b*; Bury *et al.*, 2018) was used to calculate the average diffraction-weighted doses (DWDs; Zeldin *et al.*, 2013*a*) for the data sets against which to plot the radiation damage metrics. For the dose calculations,

Table 1
Data processing and refinement statistics.

Values in parentheses are for the highest-resolution shell. The lowest-dose data set was cut to the resolution limit of the highest dose data set so that an identical set of reflections could be used for calculation of R_{free}. All the data were collected at SSRL beamline 11-1. The crystal was in space group $I222$. Number of non-H atoms = 4168 (and was not adjusted for each model), protein atoms = 3572, water molecules = 528 and ligands = 68.

Data set	1 (uncut)	1 (cut 1.17 Å)	2	3	4	5	6	7	8 (merged data)
DWD (MGy)	0.13	0.13	0.76	1.38	2.01	2.63	3.25	3.88	3.88
PDB code	6qrr	–	6qrs	6qrt	6qru	6qrv	6qrw	6qrx	6qry
Unit cell									
a (Å)	92.48	92.48	92.50	92.52	92.54	92.57	92.59	92.61	92.35
b (Å)	97.46	97.46	97.49	97.52	97.54	97.58	97.61	97.64	97.28
c (Å)	102.46	102.49	102.50	102.52	102.54	102.56	102.58	102.60	102.3
Resolution (Å)	38.69–1.096 (1.135–1.096)	38.63–1.17 (1.19–1.17)	38.69 –1.17 (1.19 –1.17)	38.70–1.17 (1.19–1.17)	38.71–1.17 (1.19–1.17)	38.72–1.17 (1.19–1.17)	39.79–1.17 (1.19–1.17)	38.74–1.17 (1.19–1.17)	39.67–1.17 (1.19–1.17)
No. of observed reflections	589885 (22614)	537565 (17750)	540859 (17728)	540378 (17781)	540698 (17818)	540867 (17745)	542096 (17827)	538263 (17654)	3770952 (125015)
No. of unique reflections	180192 (12983)	153154 (7271)	154106 (7391)	154212 (7401)	154295 (7413)	154466 (7422)	154610 (7420)	154713 (7399)	153877 (7311)
Multiplicity	3.3 (1.7)	3.5 (2.4)	3.5 (2.4)	3.5 (2.4)	3.5 (2.4)	3.5 (2.4)	3.5 (2.4)	3.5 (2.4)	24.5 (17.1)
Completeness (%)	95.7 (69.6)	99.4 (96.6)	99.4 (96.4)	99.4 (96.5)	99.4 (96.4)	99.4 (96.5)	99.4 (96.3)	99.4 (96.5)	99.8 (97.1)
Wilson *B*-factor (Å^2)	10.3	7.8	8.2	8.5	8.8	9.1	9.5	9.9	8.6
R_{meas} (%)	7.2 (43.8)	8.5 (37.2)	8.5 (42.2)	8.7 (47.6)	8.6 (53.9)	9.0 (62.3)	9.0 (73.4)	9.0 (84.7)	10.2 (55.9)
$CC_{1/2}$ (%)	99.3 (67.9)	99.4 (86.7)	99.4 (82.9)	99.3 (79.6)	99.3 (74.6)	99.3 (69.3)	99.3 (61.4)	99.3 (54.5)	99.8 (94.9)
$I/\sigma I$	10.7 (1.8)	12.2 (3.2)	11.7 (2.8)	11.3 (2.5)	11.1 (2.3)	10.5 (1.9)	10.2 (1.7)	9.9 (1.4)	23.3 (5.5)
R_{work} (%) / R_{free} (%)	12.1 / 14.7	9.8 / 11.5	9.9 / 11.7	10.0 / 11.8	10.2 / 12.0	10.5 / 12.6	10.7 / 12.6	10.9 / 12.8	9.3 / 11.0
Average *B*-factor (Å^2)	17.1	16.1	16.6	17.1	17.7	18.1	18.6	19.2	16.6
Protein	13.7	12.7	13.2	13.7	14.1	14.5	15.0	15.4	13.1
Ligands	21.7	21.6	24.2	25.3	27.4	28.0	30.0	31.3	26.3
Rmsd bond lengths (Å)	0.02	0.01	0.01	0.01	0.01	0.01	0.01	0.01	0.01
Rmsd bond angles (°)	2.3	1.2	1.2	1.2	1.2	1.2	1.2	1.2	1.2
Ramachadran plot (%)									
Favoured	96.7	96.9	96.7	97.4	97.1	97.4	97.1	97.7	97.4
Additionally allowed	2.9	2.9	2.9	2.3	2.6	2.3	2.6	2.1	2.3

knowledge of the beam (energy, flux, size and profile) along with prior knowledge of the crystal (size, shape, orientation relative to the incident beam, number of heavy atoms in solvent and protein, unit-cell parameters and the number of amino acid residues) and data collection specifics (oscillation range and exposure time) are required.

The beam shape was determined by 2D fluorescence scanning of a small cobalt crystal (∼10 µm) across the full beam, and was found to be top-hat in the horizontal direction and Gaussian in the vertical direction with a FWHM of 200 µm. Since a mixture of beam shapes cannot be used in *RADDOSE-3D* calculations, the beam profile was approximated as a Gaussian with a very large FWHM value of 2000 µm collimated to 200 µm for the horizontal direction to simulate a top-hat-shaped beam.

The beam fluxes were measured through a 200 µm × 200 µm aperture and were calculated from the ion chamber readings. The same aperture was used for the data collection. The flux was 2.2×10^{11} photons s^{-1} (before taking account of the 40% transmission used which reduced it to 8.8×10^{10} photons s^{-1}) for the complete data sets at 13 keV and 1.84×10^{11} photons s^{-1} (before taking account of the 48% transmission used which also gave 8.8×10^{10} photons s^{-1}) for the HR swathes at 14.5 keV.

The average DWDs for each complete data set were defined in a single *RADDOSE-3D* calculation so that account was taken of accumulation of DWD for the particular wedge used in the experiment. The input file contained all the complete data set wedges each separated by an HR 'burn' swathe giving a total accumulated average absorbed dose of 3.88 MGy by the end of the highest dose data set. The calculated accumulated average DWDs for the seven complete data sets were 0.13, 0.76, 1.38, 2.01, 2.63, 3.25 and 3.88 MGy. The metrics used to monitor radiation damage progression were plotted against the resulting DWD values.

2.4. MicroPIXE measurements

Since knowledge of the atomic composition of a protein is a prerequisite for the accurate calculation of the absorbed dose, the metal content of the XI sample was measured using microbeam particle induced X-ray emission (microPIXE), an established technique for such analyses (Garman & Grime, 2005). In microPIXE, the characteristic X-ray emission spectra of heavy atoms ($Z > 10$) in a protein sample are measured, which allows the stoichiometric ratios of these elements to be defined using the sulfur peak from the methionines and cysteines as an internal standard (Garman, 1999). A dried protein sample (approximate volume of solution 0.1 µl) was analysed in vacuum with a highly focused (∼1.3 µm diameter) 2.5 MeV (∼300 pA current) proton beam. The measurements were carried out at the Ion Beam Centre, University of Surrey, UK (Grime *et al.*, 1991).

Firstly, a scan over the dried drop of 750 µm × 750 µm was collected to determine the position of the protein sample. Secondly, two point spectra were recorded from different places on the sample. The sample thickness and gross matrix composition were defined by detecting the Rutherford back-scattered protons, after which the concentrations of the elements in the sample were extracted from the X-ray emission spectrum with *GUPIX* (Maxwell *et al.*, 1989) within *DAN32* (Grime, 1996) to extract the relative amount of each element, particularly manganese, in the sample.

Unfortunately, the XI E186Q sample used in the measurements was dissolved in a 0.9 *M* $(NH_4)_2SO_4$ + 1 m*M* $MgSO_4$ solution, which did not allow determination of the stoichiometric ratios of the elements due to the high extra sulfur concentration in the buffer. However, qualitatively from the microPIXE spectra we were able to determine the presence of manganese in the sample, even though no manganese was present in the reagents used in the purification or crystallization. No other metals heavier than sulfur were present. For the experimental microPIXE setup used here, magnesium was outside the detectable range of the spectrum, but the technique has the capability to detect it if a thinner beryllium filter on the Li(Si) X-ray detector is inserted. The unambiguous atomic signature from microPIXE allowed the XI metal sites to be modelled with manganese. The PIXE spectrum is shown in Fig. 2.

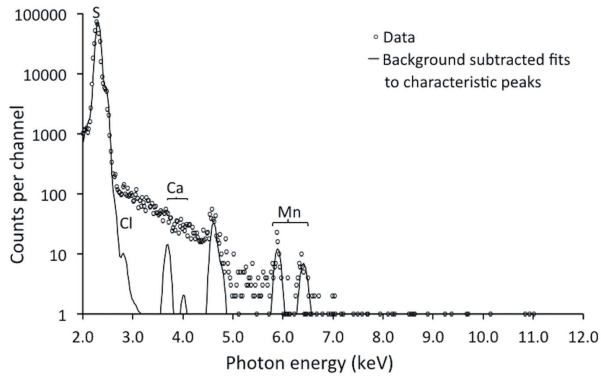

Figure 2
Spectrum of the elemental analysis of XI measured with microPIXE showing the presence of manganese, calcium, chlorine and sulfur. Note that only elements heavier than magnesium were detected in this experiment. The peak between the Ca and Mn corresponds to twice the sulfur peak energy and is due to pile-up in the Si(Li) X-ray detector of the sulfur signals.

3. Results

3.1. Global radiation damage

The data sets were analysed for global radiation damage and different metrics were plotted against the increasing absorbed average DWD. The data quality decreases strikingly linearly with dose for all metrics shown, including the exponential fit to DWD in this dose range. The results are presented in Fig. 3 and show the unit-cell volume, the relative *B*-factor ($B_{rel} = B_n - B_1$; Kmetko *et al.*, 2006) and R_{meas} increasing with dose, and $CC_{1/2}$ and the relative diffraction intensity I_n/I_1 decreasing with dose. Here, I_n is the summed total intensity for the *n*th complete data set and I_1 is the total intensity of the first low-dose data set. The total intensities were calculated from the *AIMLESS* output files as the sum of the measured reflections (N_{meas}) multiplied by the average intensities (AvI) for each resolution bin.

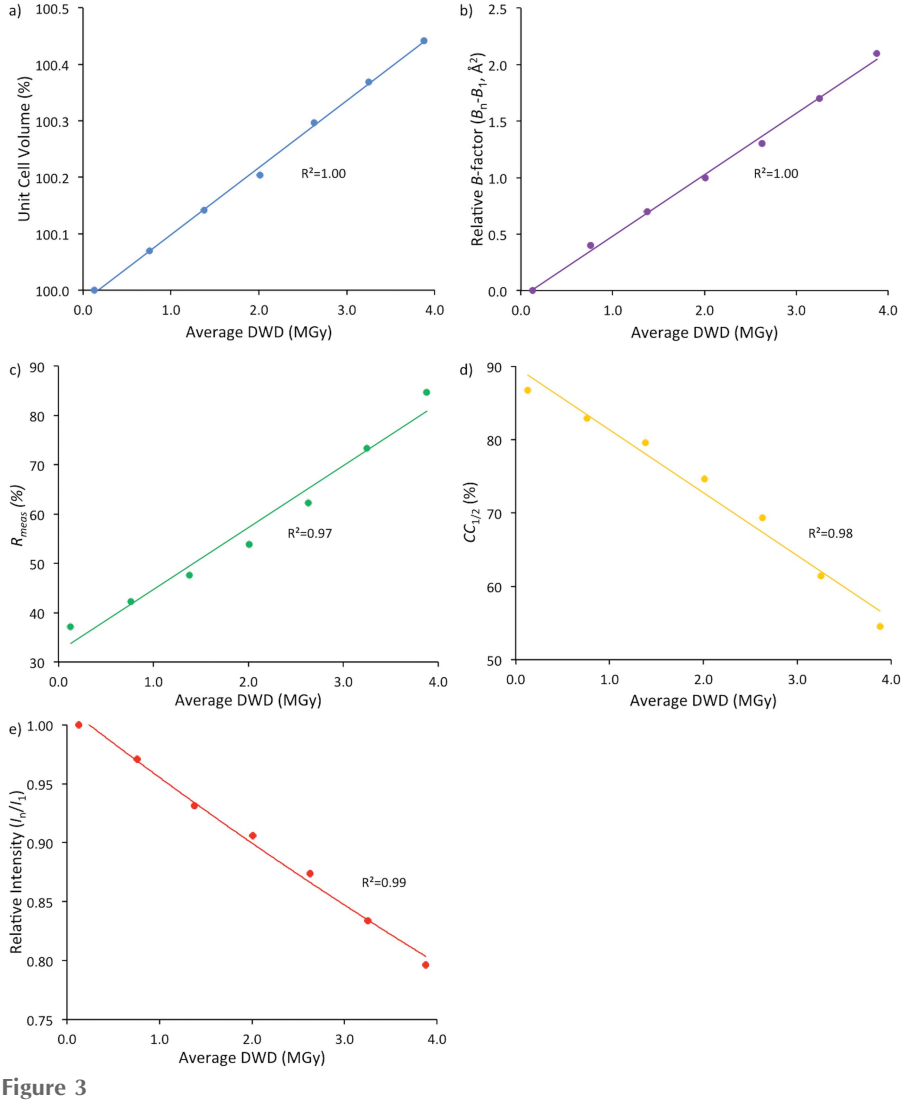

Figure 3
Radiation damage metrics and data quality indicators for the seven consecutive complete data sets as a function of dose, with linear fits shown for (*a*)–(*d*) and an exponential fit for (*e*). (*a*) The unit cell volume expands with increasing absorbed dose, as does (*b*) the relative *B*-factor and (*c*) R_{meas}, but (*d*) $CC_{1/2}$ and (*e*) the relative diffraction intensity decrease with dose.

The coefficient of sensitivity [$s_{AD} = \Delta D/(8\pi^2 \Delta B_{rel})$ where D is dose] for the XI crystal can be calculated from the gradient of the B_{rel} results, and is 0.007 Å^2 MGy^{-1}, compared with an average value of 0.012 Å^2 MGy^{-1} determined for four protein crystals at 100 K (lysozyme, thaumatin, catalase and apoferritin; Kmetko *et al.*, 2006). This value implies that the XI crystal has comparatively low sensitivity to global damage. A possible explanation of this is that there are no disulfide bonds within the structure, which are usually the most radiation sensitive species. However, the value for $D_{1/2}$, the dose to half diffraction intensity, obtained by extrapolation of the results shown in Fig. 3(*e*) is approximately 8 MGy for all data to 1.17 Å, which is in line with that observed for other proteins at 100 K. Damage to residues involved in intermolecular crystal contacts can drive the collapse of the lattice and thus a decrease in diffraction intensity, as has been observed previously for Arg–Asp contacts (Murray *et al.*, 2005).

3.2. Structure determination

The XI E186Q data sets were indexed in the orthorhombic space group *I*222 with unit-cell parameters of a = 92.5 Å, b = 97.5 Å, c = 102.5 Å for the first (lowest dose) data set. The calculated Matthews coefficient, V_M, was determined to be 2.7 Å^3 Da^{-1}, which corresponded to one monomer in the asymmetric unit and an estimated solvent content, V_S, of 54% (Matthews, 1968; Kantardjieff & Rupp, 2003). The XI monomer consists of 388 amino acid residues and all but the N-terminal methionine were present in the observed $2F_{obs} - F_{calc}$ electron density map. The final model was thus composed of 387 amino acid residues and 12 ethylene glycol, one 2-propanol and 528 water molecules, and two ions each of manganese, magnesium and sodium. Many of the amino acid residues, especially at the active site, for example the metal binding Glu217, His220, Asp255 and Asp257, had alternate conformations as described in detail below.

The structure obtained from the first (lowest dose) data set was refined to R_{work}/R_{free} values of 12.1%/14.7%, respectively. The M1 site was refined partly with an Mn^{2+} ion (occupancy 0.54) and partly a Mg^{2+} ion (occupancy 0.46) as in Munshi *et al.* (2014). This provided a good fit to the electron density. The presence of manganese and lack of any other heavy metal species (except the magnesium present in the dialysis buffer and crystallization solution) was shown with microPIXE. The Mn^{2+} at the M2 site was refined in three different conformations, M2*a*, M2*b* and M2*c* [Figs. 1 and 4(*b*)] as found in the structure used as the model-building template (PDB code: 1muw; Fenn *et al.*, 2002).

The alternate metal sites were also associated with two different conformations of residues in the active site, in particular Glu217, His220, Asp255 and Asp257, which are denoted A and B. The seven consecutive complete data sets (n = 1 to 7) were truncated to the same resolution of 1.17 Å in *AIMLESS*, because of the fall-off in resolution of the highest-dose data set. The same R_{free} test set from the lowest-dose data set was used for the higher dose data sets. The refinement statistics for the first low dose set and the following six data sets are shown in Table 1.

Following inspection of the difference maps as a function of dose, metal bond distance analysis was carried out using *COOT*, since subtle movements in active site residues were observed which were plotted against dose (see Section 3.3).

The resulting XI monomer model has a bi-domain structure, as was expected from previously deposited models [Fig. 4(*a*)]. It is formed of an N-terminal parallel $(\alpha/\beta)_8$-barrel fold (residues 2–322) and a long C-terminal loop (residues 323–387) with five α-helical segments. The active site is located at the C-terminal side of the β-barrel where both of the metal cofactors are bound in octahedral coordination in a crevice formed between the β-sheets β6, β7 and β8. XI forms a dimer by packing the active sites of two monomers together so that the barrels are coaxial. Homotetrameric quaternary structure is then formed as a dimer of dimers, in which the C-terminal extensions wrap around the adjacent monomers. Both the dimer and the tetramer have been shown to be biologically active multimers (Rangarajan *et al.*, 1992). Fig. 4(*b*) presents a close-up of the active site and the refined metal positions with their $2F_{obs} - F_{calc}$ electron density map contoured at 1σ (0.41 e$^-$ Å^{-3}).

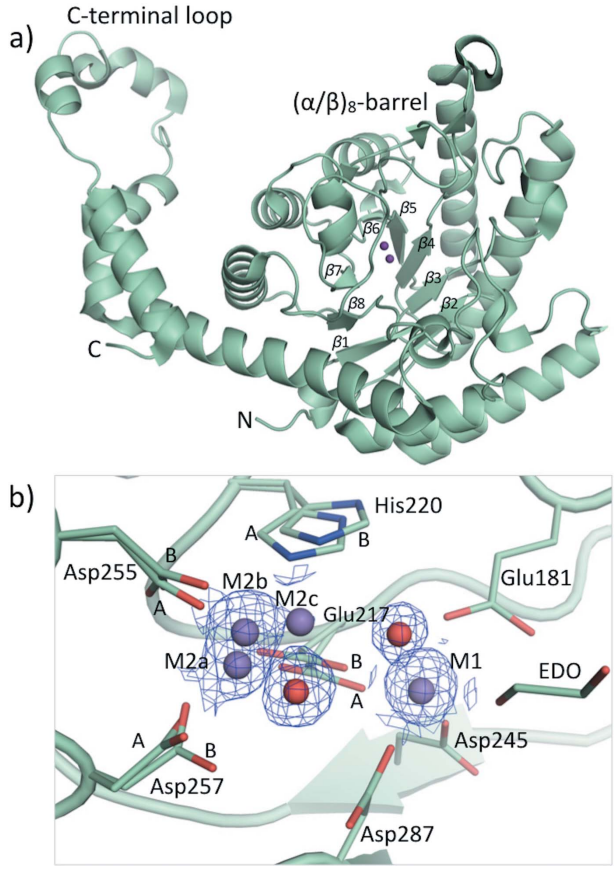

Figure 4
The structure of XI. (*a*) XI monomer showing the bi-domain arrangement: N-terminal parallel $(\alpha/\beta)_8$-barrel fold and a long C-terminal loop. (*b*) Close-up of the XI active site showing the refined metal cofactors (M1 and M2 as purple spheres, waters in red) with their $2F_{obs} - F_{calc}$ electron density map contoured at 1σ (0.41 e$^-$ Å^{-3}).

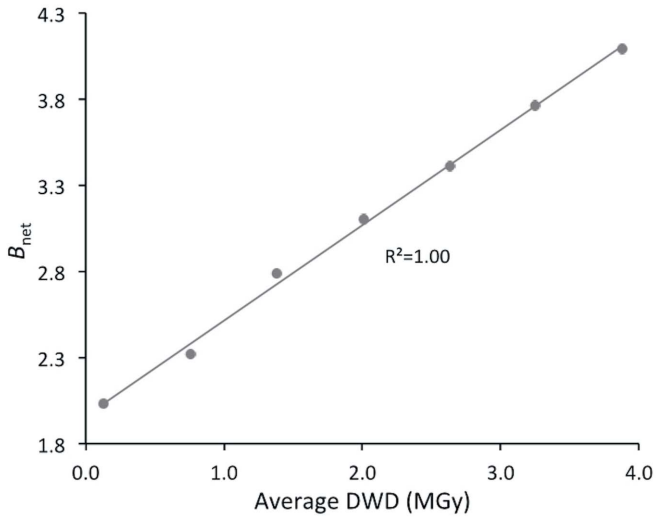

Figure 5
B_{net} (Shelley *et al.*, 2018) for the refined structures as a function of dose. B_{net}, a derivative of the B_{damage} metric (Gerstel *et al.*, 2015), which is calculated from the atomic *B*-factors corrected for packing density, summarizes in a single value the total extent of specific radiation damage and increases linearly with absorbed dose for the consecutive XI data sets.

3.3. Specific damage observations

B_{net} values for the seven structures were calculated with the *RABDAM* program (Shelley *et al.*, 2018). B_{net} is a derivative of the B_{damage} metric (Gerstel *et al.*, 2015), which is derived from the atomic *B*-factor corrected for packing density. It summarizes in a single value the total extent of site-specific radiation damage from the coordinate model associated with a single PDB entry. A linear increase in B_{net} for the structures with increasing dose was observed (Fig. 5), corresponding to the global damage effects seen in Fig. 3.

The site-specific radiation damage was analysed using the *Radiation-Induced Density Loss* program, *RIDL* (Bury *et al.*, 2017; Bury & Garman, 2018). *RIDL* calculates per-atom metrics to describe changes in electron density between structures derived from consecutive data sets. Here the D_{loss} metric, calculated as the maximum electron density loss compared with the lowest dose structure in the local region around each atom in XI for each higher data set's $F_{obs,n} - F_{obs,1}$ Fourier difference map, has been used as a per-atom indicator of site-specific damage with increasing dose.

In Fig. 6 the top 25 D_{loss} sites calculated by *RIDL* are presented as red spheres, with the radius of each sphere being proportional to the magnitude of D_{loss}. Figs. 6(*a*) and 6(*b*) present the top 25 specific damage sites identified by the $F_{obs,2} - F_{obs,1}$ and $F_{obs,7} - F_{obs,1}$ maps, respectively. The increase in damage with dose, at the active site and the surroundings of the catalytic metals, can clearly be seen. For the $F_{obs,2} - F_{obs,1}$ map [see Fig. 6(*a*)] of the 25 most damaged residues, the greatest indication of damage was associated with the M2 site, with the majority of the other sites shown being related to Met residues, and to those residues having multiple conformations.

For the 25 most affected residues seen in the $F_{obs,7} - F_{obs,1}$ map [Fig. 6(*b*)], the sites are those expected to be damaged, with the greatest D_{loss} again appearing at the active site. For multiple conformations, *RIDL* removes all but the highest-occupancy conformation and performs its analysis on that conformation. Because two conformations of the active site exist, the lower occupancy *B* conformation was examined by removing the A conformation before running *RIDL* a second time. However, since the D_{loss} metric in *RIDL* did not appear sensitive to the very small structural changes in the active site, the D_{loss} analysis was only performed for the highest occupancy state.

Top locations of site-specific damage for the $F_{obs,7} - F_{obs,1}$ map include the catalytic metal, the sulfurs of methionine side chains, the oxygen atoms of aspartic and glutamic acids around the active site and the multimer forming surfaces of XI. Furthermore, oxygen atoms of water molecules, ethylene glycols and the side chains of glutamine, serine and threonine appear on the list of damaged sites. XI has no disulfide bonds. Even for radiation-insensitive atoms the damage is observed to increase with dose owing to the increasing noise in the $F_{obs,n} - F_{obs,1}$ map caused by the decreasing diffraction data quality.

Isomorphous difference Fourier maps (calculated by *RIDL*) for the active site are presented for $F_{obs,2} - F_{obs,1}$ in Figs. 7(*a*) and 7(*b*) (negative/positive difference density, respectively), and for $F_{obs,7} - F_{obs,1}$ in Figs. 7(*c*) and 7(*d*) (negative/positive

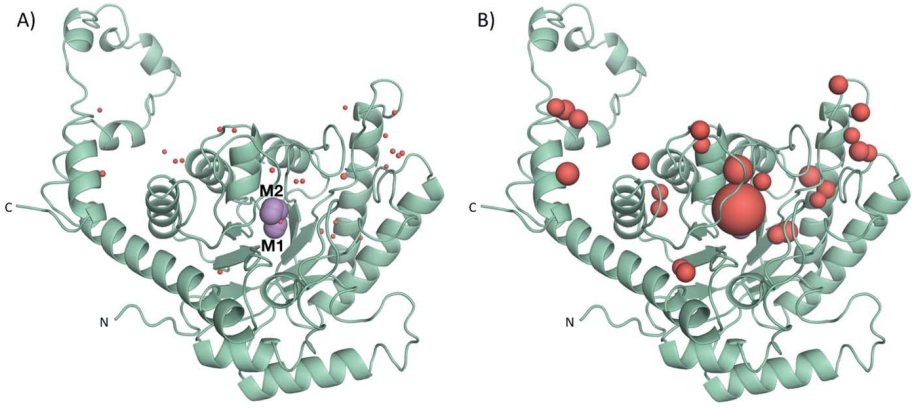

Figure 6
Top 25 specific damage sites calculated by *RIDL* (Bury & Garman, 2018) and presented as red spheres. The radius of each sphere is proportional to the D_{loss} metric calculated by *RIDL*, which indicates the maximum electron density loss in the local region of each atom in XI for the $F_{obs,n} - F_{obs,1}$ Fourier difference map associated with each higher dose data set *n*. (*a*) The specific damage sites for $F_{obs,2} - F_{obs,1}$ and (*b*) for $F_{obs,7} - F_{obs,1}$. The increase in the damage with increasing dose is clearly visible, especially at the active site and the surroundings of the catalytic (M2) and stabilizing (M1) metals which are shown as violet spheres. For those residues with dual conformations, the highest occupancy positions were analysed.

difference density, respectively). Both positive and negative difference density is observed around the three M2 metal sites and clear negative density on the oxygen atoms of the glutamates and aspartates, in line with usual observations of specific damage in MX. The single conformation of the residues in the active site shows the A conformation, with the lower occupancy B conformation being removed as part of the *RIDL* processing.

For the lowest-dose interval, the $F_{obs,2} - F_{obs,1}$ electron density data, Figs. 7(*a*) and 7(*b*), show electron density loss around Glu217 (OE2 and CD atoms), as well as Asp257 (OD1 and OD2 atoms). This corresponds to the decarboxylation of the acidic side chains noted in many studies on radiation damage. There is no corresponding positive density for the side chains, largely ruling out any coordinated shift in atom positions. The catalytic metal M2 in position M2*a* shows a reduction in electron density, and a gain around positions M2*b* and M2*c*. This is not reflected in an occupancy change (see Table 2). There is loss of electron density around the O1 and O2 atoms of ethylene glycol and the water molecule next to M2*a*. For the highest dose interval, the $F_{obs,7} - F_{obs,1}$ electron density maps in Figs. 7(*c*) and 7(*d*) show both local gain and loss of density. Both OD1 and OD2 atoms of Asp245, Asp255 and Asp287 see a decrease in density, as well as OE2 of Glu181 and OE1 of Glu217, and the bond between His220 NE2 and CE1 atoms. It is also noteworthy that the M1 position and the water molecule adjacent to it lose electron density.

As detailed in Table 2, only slight changes are seen in the occupancies of the alternate conformations of the catalytic metal M2 and the active site residues, indicating that the changes in the electron density as a function of dose are not a consequence of conformational changes. Analysis of the M2 isotropic *B*-factor shows an increase for M2*a* from 6.7 to 14.6 Å^2, for M2*b* from 7.2 to 12.1 Å^2, and M2*c* a decrease from 10.4 to 7.7 Å^2. This suggests disorder increasing in the M2*a* and M2*b* sites with order in the M2*c* site improving with dose.

No movement in metal position is observed as a function of dose. Table 3 shows changes in the absolute position of the M2 metal site. M2*a* undergoes a shift of 0.17 Å, M2*b* of 0.08 Å and M2*c* of 0.10 Å. However, when the absolute coordinates are converted to fractional coordinates the changes in metal positions are negligible from lowest to highest dose, being

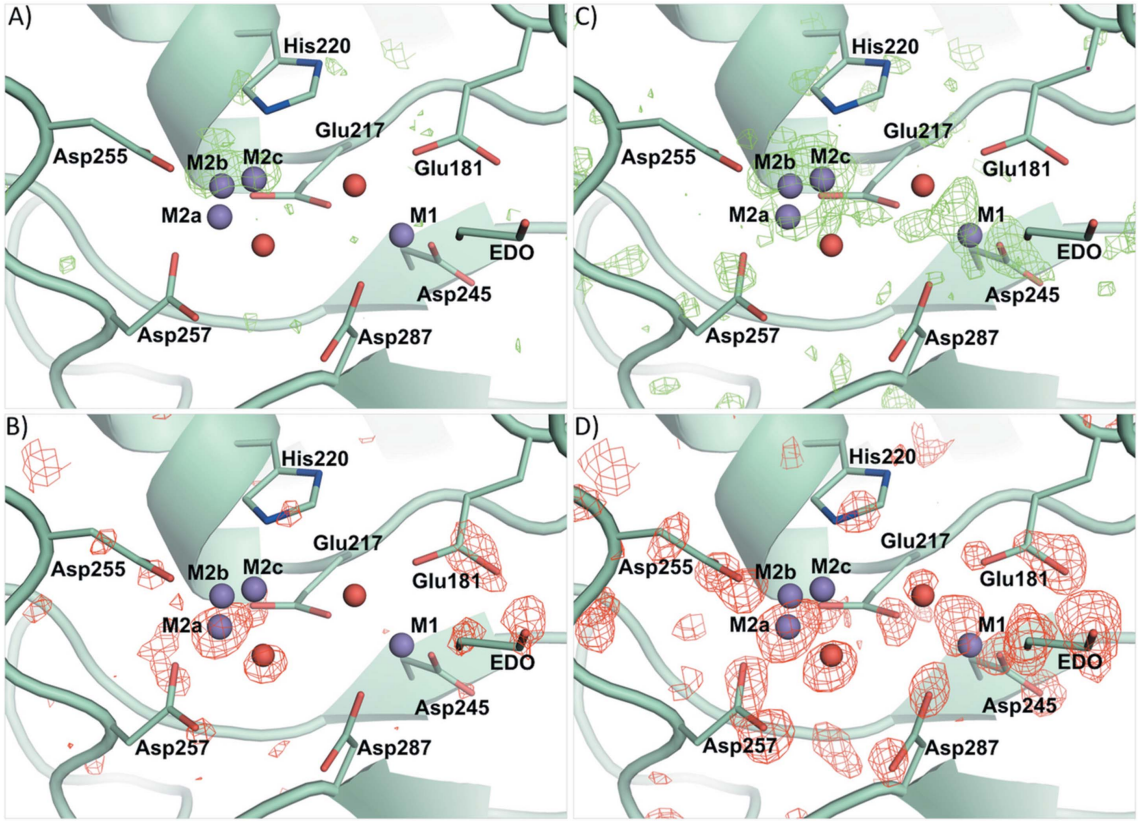

Figure 7
Fourier difference density maps of the active site of XI calculated using *FFT* (Ten Eyck, 1973) through the *RIDL* pipeline (Bury & Garman, 2018). Here, each $F_{obs,n} - F_{obs,1}$ map has been calculated using the observed structure factor amplitudes $|F_{obs,n}|$ and $|F_{obs,1}|$ associated with data sets n and 1, respectively, using the calculated phase set corresponding to the 0.13 MGy low-dose refined coordinate model. The $F_{obs,n} - F_{obs,1}$ maps represent the electron density loss between the lowest-dose data set and each higher-dose data set $n > 1$. (*a*, *b*) Difference density maps for $F_{obs,2} - F_{obs,1}$ contoured at $\pm 3\sigma$ (0.07 e$^-$ Å^{-3}), (*c*, *d*) for $F_{obs,7} - F_{obs,1}$ (negative/positive difference densities in red/green, respectively). The increase in damage with increasing dose, especially at the active site and the surroundings of the catalytic metals, is clear. The difference density maps also reflect visually how the electron density around the catalytic metal ion changes. The conformation with the highest occupancy, A, is used by *RIDL* but, as mentioned in the text, the *RIDL* analysis is not sensitive enough to detect the radiation damage associated with the small structural changes seen between A and B conformations.

Table 2
Occupancies of the catalytic metal M2 and alternate conformations of active site amino acid residues as a function of dose.

				Glu 217		His 220		Asp 255		Asp 257	
DWD (MGy)	M2*a*	M2*b*	M2*c*	A	B	A	B	A	B	A	B
0.13	0.41	0.55	0.04	0.13	0.87	0.32	0.68	0.42	0.58	0.38	0.62
0.76	0.44	0.52	0.04	0.14	0.86	0.36	0.64	0.37	0.63	0.35	0.65
1.38	0.41	0.55	0.04	0.13	0.87	0.33	0.67	0.39	0.61	0.33	0.67
2.01	0.41	0.54	0.05	0.14	0.86	0.31	0.69	0.40	0.60	0.35	0.65
2.63	0.40	0.55	0.05	0.14	0.86	0.33	0.67	0.33	0.65	0.37	0.63
3.25	0.42	0.51	0.07	0.13	0.87	0.31	0.69	0.37	0.63	0.34	0.66
3.88	0.46	0.50	0.04	0.14	0.86	0.33	0.67	0.38	0.62	0.38	0.62

Table 3
Absolute and fractional coordinates of the M2*a*, M2*b* and M2*c* positions as a function of dose.

Fractional dose is given to three decimal places to indicate slight changes.

	Absolute position (Å)			Fractional position		
DWD (MGy)	*x*	*y*	*z*	*x*	*y*	*z*
M2*a*						
0.13	7.55	35.19	43.79	0.082	0.380	0.474
0.76	7.57	35.21	43.86	0.082	0.381	0.474
1.38	7.57	35.24	43.87	0.082	0.381	0.474
2.01	7.59	35.26	43.93	0.082	0.381	0.475
2.63	7.59	35.26	43.93	0.082	0.381	0.475
3.25	7.62	35.33	44.04	0.082	0.382	0.476
3.88	7.64	35.33	44.05	0.082	0.382	0.476
M2*b*						
0.13	7.80	35.57	44.47	0.080	0.365	0.456
0.76	7.80	35.63	44.52	0.080	0.365	0.457
1.38	7.79	35.63	44.55	0.080	0.365	0.457
2.01	7.80	35.67	44.58	0.080	0.366	0.457
2.63	7.80	35.69	44.59	0.080	0.366	0.457
3.25	7.81	35.72	44.63	0.080	0.366	0.457
3.88	7.77	35.75	44.62	0.080	0.366	0.457
M2*c*						
0.13	9.05	35.21	44.85	0.088	0.344	0.438
0.76	9.00	35.27	44.91	0.088	0.344	0.438
1.38	9.02	35.29	44.92	0.088	0.344	0.438
2.01	8.99	35.34	44.96	0.088	0.345	0.438
2.63	9.03	35.33	44.95	0.088	0.344	0.438
3.25	9.01	35.33	44.98	0.088	0.344	0.438
3.88	8.98	35.35	44.96	0.088	0.345	0.438

0.008, 0.004 and 0.004 for M2*a*, M2*b* and M2*c*, respectively, on a normalized scale. These absolute changes are compatible with the 0.13 Å, 0.18 Å and 0.14 Å expansion in the *a*, *b* and *c* parameters of the unit cell over a dose of 3.88 MGy and might partly explain the electron density loss seen around M2*a* and gain around M2*b* and M2*c* (see Fig. 7, produced without consideration of the cell parameter change).

Residues associated with the M2 metal positon are Glu217, His220, Asp255 and Asp257. M2*a*, M2*b* and M2*c* maintain a fairly constant bond distance to Glu217 in both the A and B conformations. The metal occupancies did not vary significantly as a function of dose with M2*a*, M2*b* and M2*c* having average occupancies of 0.42, 0.53 and 0.05, respectively, and standard deviations over the set of 0.02, 0.02 and 0.01. Similarly, both the A and B conformations of Glu217, His220, Asp255 and Asp277 maintained fairly constant occupancies during the dose series. For conformation A, this was 0.14, 0.33, 0.38 and 0.36, and, for conformation B, 0.86, 0.67, 0.62 and 0.64, respectively. Glu217 occupancy in the B conformation is closely related to the sum of the M2*a* and M2*b* occupancies, whereas those of conformation A for His220, Asp255 and Asp257 closely match that of M2*a*, and B conformations of the same residues are a closer match to the M2*b* occupancy. Glu217 in the A conformation seems more closely associated with the occupancy of M2*c*. This can be seen in Fig. 8. The residues involved in the proton transfer reaction, His54 and Lys289 are not bonded to either M1 or M2.

Metal bonding distances are shown in Table 4 with their standard deviations for high-resolution protein structures (Zheng *et al.*, 2008), as well as the error in the atomic coordinate (Kumar *et al.*, 2015) for the bonding atoms. Bond distance decreases from the lowest to highest dose for Asp225 OD2 conformation A to M2*a*, but no significant change is seen for conformation B to M2*b* or M2*c*. The Asp257 bond distance to M2*a*, M2*b* and M2*c* is fairly stable for both A and B conformations. It can be seen visually that M2*a* matches conformation A and M2*b* matches conformation B. His220 appears to shift closer to M2*b* and closest to M2*c* in the A conformation.

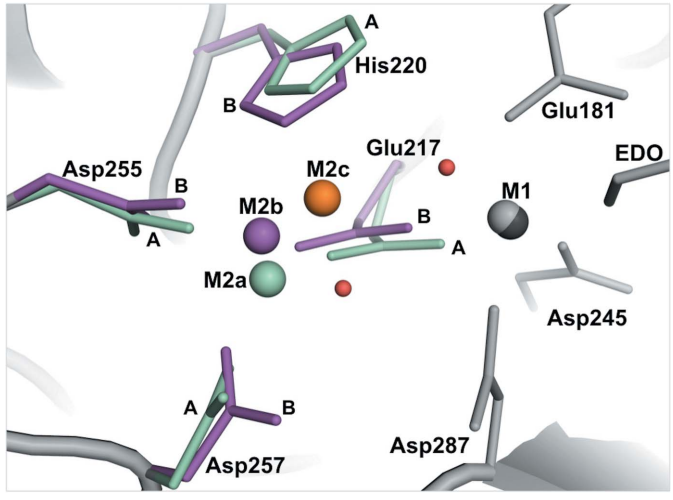

Figure 8
Details of the three M2 positions and the alternate residue conformations, A and B, shown in green and violet respectively. Waters are also shown in red. Residues with no alternate conformations are coloured grey. The three metal positions M2*a*, M2*b* and M2*c* are coloured green, violet and orange, respectively.

Table 4
Active-site metal bonding distances for the lowest- and highest-dose structures with the coordinate error (Kumar *et al.*, 2015) for the bonding atoms.

Distances, including the coordinate error (CE), are given in Å. No *B* conformation is given if the distances are above three standard deviations from an expected bond length. Bonds within one standard deviation of expectations (Zheng *et al.*, 2008) are shown in bold, those with two standard deviations in italic, and finally those within three standard deviations, unlikely to be bonds, not highlighted at all. A difference is clearly seen between low and high doses for M2*a* and M2*c*, compared with M2*b*. The differences are significant when compared with the errors indicated by the precision of the atomic coordinates.

	Lowest DWD 0.13 MGy						Highest DWD 3.88 MGy					
	M1Mn	M1Mg	M2*a*	M2*b*	M2*c*	CE	M1Mn	M1Mg	M2*a*	M2*b*	M2*c*	CE
Conformation A												
Glu181(OE2)	**2.08**	**2.01**				0.013	**2.09**	**2.00**				0.017
Asp245(OD2)	*1.95*	**2.05**				0.014	*1.92*	**2.07**				0.017
Asp287(OD2)	**2.01**	**2.05**				0.013	**2.02**	**2.09**				0.017
EDO1(O2)	**2.17**	**2.23**				0.014						0.019
HOH148	*2.44*	2.33				0.016	**2.36**	**2.24**				0.022
Glu217(OE1)	1.72	1.68				0.011	1.78	1.55				0.013
Glu217(OE2)			**2.09**	**2.15**	**2.17**	0.010			**2.13**	**2.27**	**2.22**	**0.013**
His220(NE2)			3.73	2.99	**2.21**	0.011			3.46	2.85	**2.15**	**0.014**
Asp255(OD2)			*1.98*	1.66	2.62	0.013			*1.85*	1.54	2.51	0.017
Asp257(OD1)			*1.86*	2.59	2.69	0.014			*1.90*	2.51	3.50	0.015
HOH38			*1.94*	**2.23**	**2.02**	*0.015*			*1.92*	**2.29**	**1.96**	**0.019**
Conformation B												
Glu217(OE1)	**2.13**	**2.05**				0.013	**2.25**	**1.97**				0.016
Glu217(OE2)			**2.04**	**2.00**	**2.33**	0.012			**2.04**	**2.01**	**2.30**	**0.015**
His220(NE2)			3.06	**2.29**	1.83	0.012			2.87	**2.22**	1.81	0.015
Asp255(OD1)			2.61	**2.26**	3.41	0.013			2.59	**2.21**	3.37	0.015
Asp255(OD2)			2.62	**2.24**	2.90	0.014			2.61	**2.27**	2.91	0.016
Asp257(OD1)			1.6	**2.30**	3.44	0.014			1.80	*2.34*	3.43	0.017

Active site residue atom distances are plotted as a change in length as a function of dose in Fig. 9. The figure breaks down the distances to M2*a*, M2*b* and M2*c* and residue A and B conformations. Fig. 9(*a*) shows that Asp255 OD2 increases in distance from M2*a* while OD1 shifts toward M2*a* in conformation A. This is a subtle change which appears to be due to rotation of the terminal part of the residue. A more pronounced change is evident for His220 NE2 which shifts almost 0.3 Å towards M2*a*. Given that the unit cell is expanding as a function of dose, any motion that reduces distances is likely to be a result of specific radiation chemistry effects rather than of global damage. Glu217 and Asp257 show an increase in distance from M2*a* in conformation A. For conformation B [see Fig. 9(*b*)], the distance between His220 and M2*a* is still decreasing with dose, whereas Asp257 OD1 is increasing in distance and all other residue atoms remain at a fairly constant distance.

For M2*b* [see Fig. 9(*c*)], there are small changes seen for conformation A, but less than the almost 0.3 Å for His220. The results are similar for M2*c* and conformation A [see Fig. 9(*e*)]. For M2*b* and M2*c*, there are minimal distance changes for residue conformation B [see Figs. 9(*d*) and 9(*f*)]. The structural model is an average of all the unit cells in the crystal and the occupancy table thus describes the overall composition of that crystal. The distance and occupancy results suggest that the A residue conformation is driven to the B conformation by dose and that the B conformation is associated with M2*b* and M2*c*. Glu217 distances appear to be constant in both the A and B conformations. M2*a* is not bonded to His220 and has a distance of 3.46 Å at the highest dose but is bonded to M2*b* in the B conformation and very closely bonded to M2*c*. H220 NE2 shows an almost linear decrease in distance to M2*a* with dose.

RIDL also outputs a metric called $D_{\rm neg}$ which is essentially a measure of the average $F_{{\rm obs},n} - F_{{\rm obs},1}$ negative density surrounding each atom, where the contribution of each voxel's value to the $D_{\rm neg}$ metric is weighted by the relative proportion of actual electron density corresponding to the atom at that position. This provides an indication of the magnitude of electron density lost with increasing dose for each atom (similar to the $D_{\rm loss}$ metric) but it up-weights negative density changes close the centre of mass of each atom and down-weights negative density changes further from the centre of mass of each atom. As such, it is more sensitive to the small spatial changes indicated for active site residue conformations A and B.

Fig. 10 shows $D_{\rm neg}$ for the residues associated with M2 for both the A [Fig. 10(*a*)] and B [Fig. 10(*b*)] conformations. The damage seems similar with the only noticeable difference being the increased sensitivity of Asp257 OD2 in the B conformation. Asp257 shows a significant twist in the B conformation and this damage indicator may explain that twist. His220 is twice as sensitive to damage in the A conformation than when in the B position. Glu217 and Asp255 show similar sensitivity in both the A and B conformations. The OD2 of Asp257 is about three times as sensitive in the B conformation as the A conformation. For comparison, in Fig. 10(*c*), Asp80, one of the residues involved in the tetramer crystal contacts is shown on the same scale. The main chain atoms show little damage and the side chain shows an almost linear effect with dose.

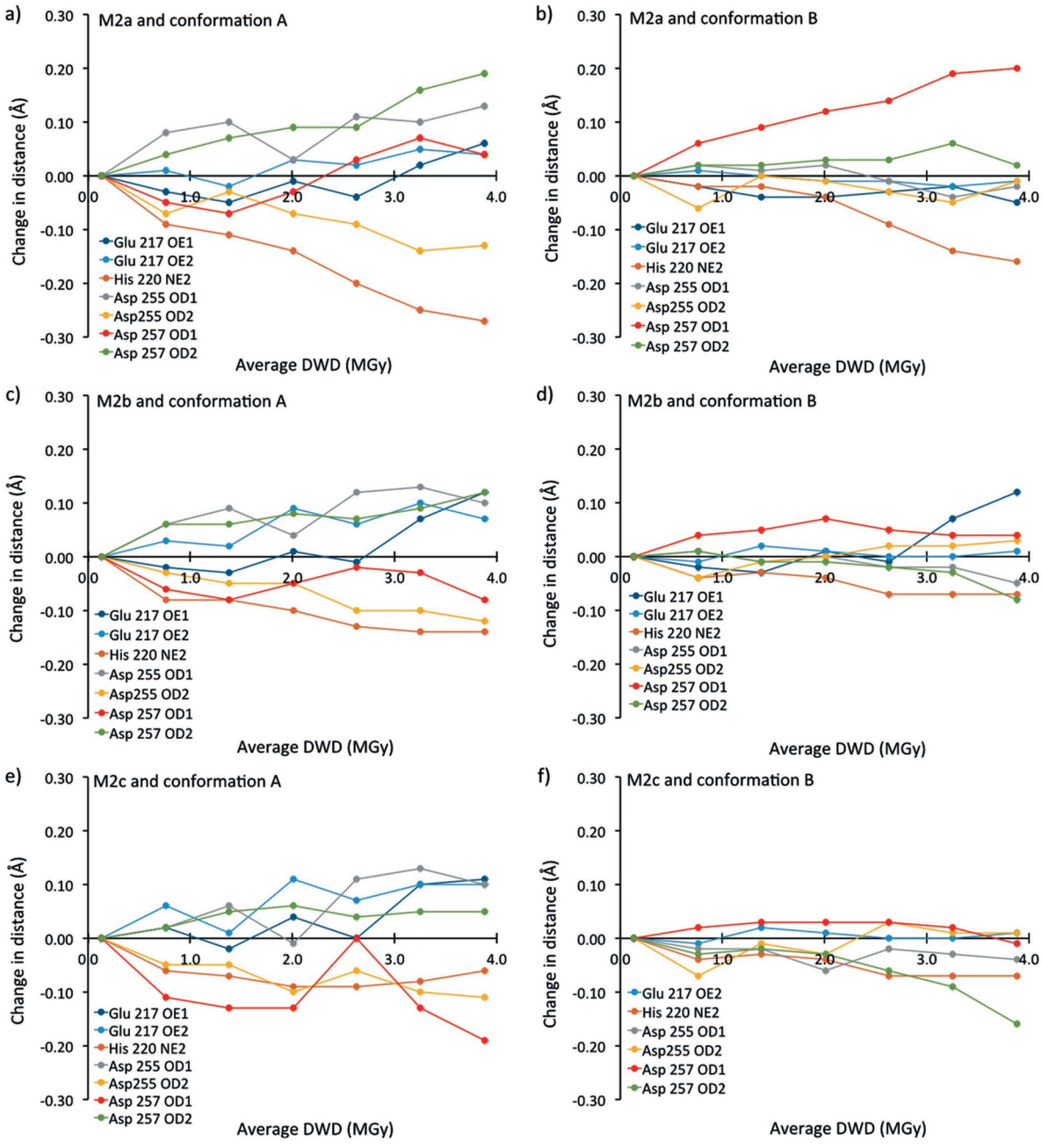

Figure 9
Relative change in distance between residues in the active site and M2 metal positions in conformation A and conformation B for M2*a* (*a*, *b*), M2*b* (*c*, *d*) and M2*c* (*e*, *f*). All graphs are plotted on the same scale so that significant distance changes are easily seen.

4. Discussion

As the results presented above indicate, both the global and site-specific radiation damage to the XI crystal progress linearly with dose over the dose range studied here (0.13–3.88 MGy). Considering that the highest dose is only 3.88 MGy, the site-specific damage is significant: the difference density map calculated for the lowest-dose data sets $F_{obs,2} - F_{obs,1}$ [Figs. 7(*a*) and 7(*b*)] already shows negative difference density around the M2*a* position, acidic side chains, and water and ethylene glycol molecules at the active site. The difference density significantly increases with dose (Fig. 7) showing clearly, for example, that the decarboxylation of acidic side chains is taking place around Asp245, Asp255, Asp257, Asp287 and Glu181.

The increase in site-specific damage is observable from inspection of the top 25 damage sites (Fig. 6), despite the fact that the dose is only 3.88 MGy. This is far lower than the experimental radiation dose limit of 30 MGy determined for cryo-cooled protein crystals beyond which it was judged biological information could be compromised (Owen *et al.*, 2006). XI is a tetramer in the unit cell, with Asp80, Thr82, Arg331, Asp336 and Arg340 forming crystal contacts between the separate tetramers. The crystal contacts associated with

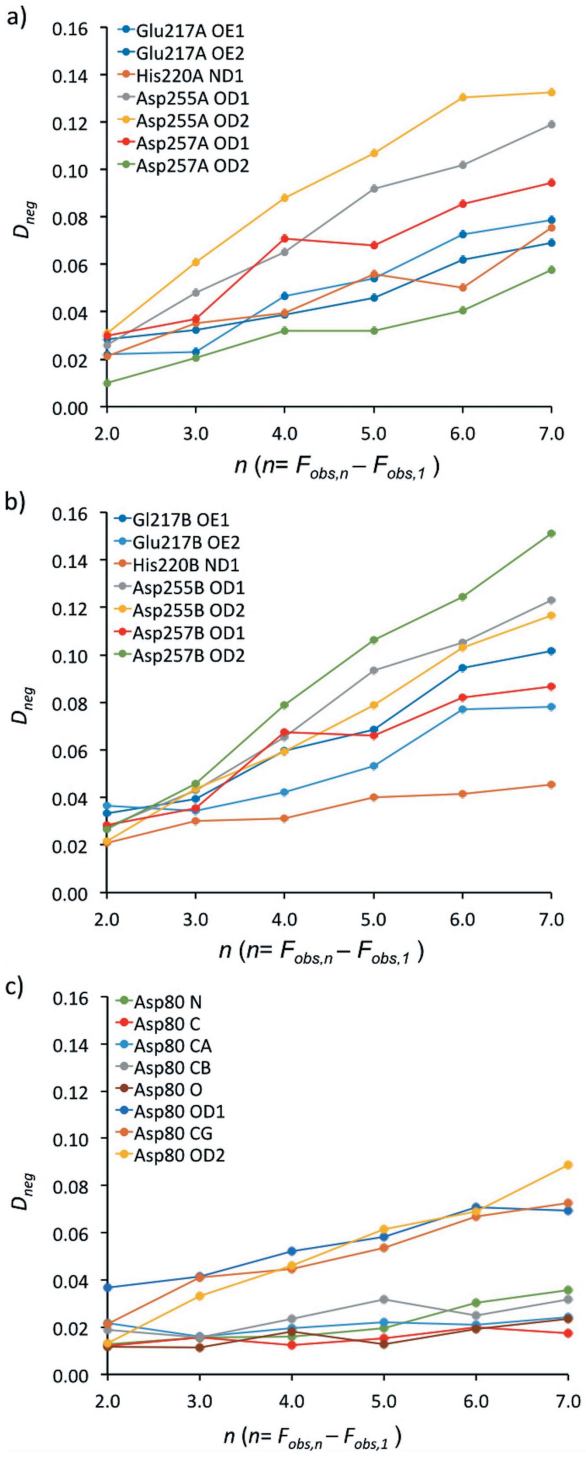

Figure 10
Plots of D_{neg} for the A and B residue conformations, plots (*a*) and (*b*), respectively, in the M2 active site shown compared with Asp80 in plot (*c*), one of the residues associated with the XI tetramer crystal contacts.

Asp may increase the sensitivity of the crystal lattice to damage, although the trends seen in Fig. 10(*c*) suggest that this damage takes place at a lower rate than that occurring in the active site.

The detailed analysis of the changes in the XI active site with dose presented above raises two pertinent questions in relation to the interpretation of active site changes during the mechanistic and structural analysis of metalloproteins.

Firstly, several papers in the literature report a movement of the XI M2 metal positions which was hypothesized to be associated with the catalysis mechanism (Collyer *et al.*, 1990; Jenkins *et al.*, 1992; Bogumil *et al.*, 1997; Asbóth & Náray-Szabó, 2000; Lavie *et al.*, 1994; Fenn *et al.*, 2004). Here, we indeed observed an absolute movement of the metals with increasing dose. However, once the radiation-induced unit-cell expansion has been taken into account by conversion of the metal positions to fractional coordinates, this disappears within error. We thus conclude that the metals do not shift.

Note that in our work the M2 site occupancies do not change with dose either, and that our values are at variance with those of Fenn *et al.* (2002) where for the ligand-free model 1MUW, M2*a*, M2*b* and M2*c* have occupancies of 0.69, 0.48 and 0.16 compared with those here of 0.42, 0.53 and 0.05. In other XI structural models, there are occupancies of less than unity for the M2 position. It is possible that lack of knowledge of the exact identity of the metal or metals in the M2 site may explain some of these results or that the reduction of the metal by free radicals produced from X-ray irradiation could impact occupancy calculations. Given the importance of the metal site in the enzymatic mechanism and the observation that many structures have over-occupied or under-occupied states, accurate knowledge of both the identity of the metal and radiation chemistry effects is a critical element of understanding mechanism.

Secondly, although the unit-cell volume expands with dose, we observe that two distances to the M2*a* metal site decrease by small but significant amounts, and that they behave differently for conformations A and B: those of His220 NE2 (3.73 Å to 3.46 Å) and of Asp255 OD2 to (1.98 Å to 1.85 Å); see Fig. 8. Asp255 OD2 is explained by a rotation of the residue but His220 shifts toward M2*a*. The D_{neg} metric from *RIDL* is sensitive to the His220 and Asp255 rotation. The bond lengths for other residues in the active site remain reasonable static with the possible exception of His220 to M2*b* with a small reduction going from 2.29 Å to 2.22 Å.

A study of four active site mutants of the His220 residue (His220Ser, His220Glu, His220Asn and His220Lys) in the XI (Cha *et al.*, 1994) M2 octahedral coordination sphere concluded that the His220 residue was vital for enzyme activity. The k_{cat} values decreased to 0.3–0.5% of the wild-type values for His220Ser, His220Asn and His220Glu, and the K_m values increased 30–40-fold. His220Lys was inactive. The metal binding was perturbed by replacing His220 and the mechanism disrupted. Thus, His220 appears to fulfil a pivotal role for the XI enzyme. Here, we observe it moving towards the M2a site.

An explanation of this could be hypothesized from the radiation chemistry. Metals are reduced by the X-ray beam and become negatively charged. The crystallization conditions have a pH of 7.0, and the pK_a of His is 6.0. At zero dose, the His is uncharged. Free radical production will lower the pH and, if it decreases to the pK_a value or below, a positive charge will be generated on the His and thereby produce an attractive

force toward the reduced metal. The rotation of the Asp is probably a combination of the metal reduction and decarboxylation of the residue. Thus, radiation chemistry could be driving these changes in the enzymatic active site.

Our study shows that the M2*c* position is real, and is seen in the unliganded protein at low occupancy. The native protein has three M2 positions and two alternate residue conformations in the active site. M2*a* is associated with one of these, and M2*b* and M2*c* with the other. Glu217 remains at a constant distance from both M2*a* and M2*b*. Radiation chemistry could be mimicking mechanism, but without substrate and product studied in a similar manner it is not possible to conclude this.

The mechanism of action of the XI enzyme has been the subject of discussion for many years and involves the three catalytic metal sites. From the analysis reported above, our hypothesis is that the elusiveness of the mechanism has been confounded by radiation chemistry. Our results showed a motion of the metals in absolute space. This could be interpreted as mechanistically important when comparing models determined with different effective X-ray doses. However, a fractional coordinate analysis showed that it was simply driven by the expansion of the unit cell, a well known result of global radiation damage.

In summary, this study highlights once again the need to be aware of, and take into account, the various effects of radiation damage when interpreting structures mechanistically, particularly for metalloproteins where even a low dose structure can be perturbed by the radiation chemistry induced around the metal binding site. While the changes seen are small, our results show that both global and specific damage can have a potential impact on structural interpretation.

Acknowledgements

Kristin A. Sutton, Ana González, Kathryn L. Shelley and Joshua L. Dickerson are thanked for the various contributions to this work. Stanford Synchrotron Radiation Lightsource (SSRL, Stanford, USA) and the staff of beamline 11-1 are gratefully acknowledged. The contents of this publication are solely the responsibility of the authors and do not necessarily represent the official views of NIGMS or NIH. We also gratefully acknowledge the Surrey Ion Beam Centre and Geoff Grime for assistance with the PIXE measurements.

Funding information

Use of the SSRL, SLAC National Accelerator Laboratory, is supported by the US Department of Energy, Office of Science, Office of Basic Energy Sciences under Contract No. DE-AC02-76SF00515. The SSRL Structural Molecular Biology Program is supported by the DOE Office of Biological and Environmental Research, and by the National Institutes of Health, National Institute of General Medical Sciences (including P41GM103393). Also, the UK Engineering and Physical Sciences Research Council (grant No. EP/G03706X/1) for studentship funding in the Systems Biology Programme of the University of Oxford Doctoral Training Centre (CBS). This work was supported by the Finnish Cultural Foundation and the NSF BioXFEL Center (grant 1231306 to EHS).

References

Adams, P. D., Afonine, P. V., Bunkóczi, G., Chen, V. B., Davis, I. W., Echols, N., Headd, J. J., Hung, L.-W., Kapral, G. J., Grosse-Kunstleve, R. W., McCoy, A. J., Moriarty, N. W., Oeffner, R., Read, R. J., Richardson, D. C., Richardson, J. S., Terwilliger, T. C. & Zwart, P. H. (2010). *Acta Cryst.* D**66**, 213–221.
Afonine, P. V., Grosse-Kunstleve, R. W., Echols, N., Headd, J. J., Moriarty, N. W., Mustyakimov, M., Terwilliger, T. C., Urzhumtsev, A., Zwart, P. H. & Adams, P. D. (2012). *Acta Cryst.* D**68**, 352–367.
Allen, K. N., Lavie, A., Glasfeld, A., Tanada, T. N., Gerrity, D. P., Carlson, S. C., Farber, G. K., Petsko, G. A. & Ringe, D. (1994). *Biochemistry*, **33**, 1488–1494.
Asbóth, B. & Náray-Szabó, G. (2000). *Curr. Protein Pept. Sci.* **1**, 237–254.
Berman, H., Henrick, K. & Nakamura, H. (2003). *Nat. Struct. Mol. Biol.* **10**, 980.
Berman, H., Westbrook, J., Feng, Z., Gilliland, G., Bhat, T., Weissig, H., Shindyalov, I. & Bourne, P. (2000). *Nucleic Acids Res.* **28**, 235–242.
Bhosale, S. H., Rao, M. B. & Deshpande, V. V. (1996). *Microbiol. Rev.* **60**, 280–300.
Blow, D. M., Collyer, C. A., Goldberg, J. D. & Smart, O. S. (1992). *Faraday Disc.* **93**, 67–73.
Bogumil, R., Kappl, R., Hüttermann, J. & Witzel, H. (1997). *Biochemistry*, **36**, 2345–2352.
Bowman, S. E., Bridwell Rabb, J. & Drennan, C. L. (2016). *Acc. Chem. Res.* **49**, 695–702.
Burmeister, W. P. (2000). *Acta Cryst.* D**56**, 328–341.
Bury, C. S., Brooks-Bartlett, J. C., Walsh, S. P. & Garman, E. F. (2018). *Protein Sci.* **27**, 217–228.
Bury, C. S., Carmichael, I. & Garman, E. F. (2017). *J. Synchrotron Rad.* **24**, 7–18.
Bury, C. S. & Garman, E. F. (2018). *J. Appl. Cryst.* **51**, 952–962.
Callens, M., Kersters-Hilderson, H., Van Opstal, O. & De Bruyne, C. K. (1986). *Enzyme Microb. Technol.* **8**, 696–700.
Carrell, H. L., Rubin, B. H., Hurley, T. J. & Glusker, J. P. (1984). *J. Biol. Chem.* **259**, 3230–3236.
Carugo, O. & Djinović Carugo, K. (2005). *Trends Biochem. Sci.* **30**, 213–219.
Cha, J., Cho, Y., Whitaker, R. D., Carrell, H. L., Glusker, J. P., Karplus, P. A. & Batt, C. A. (1994). *J. Biol. Chem.* **269**, 2687–2694.
Chen, V. B., Arendall, W. B., Headd, J. J., Keedy, D. A., Immormino, R. M., Kapral, G. J., Murray, L. W., Richardson, J. S. & Richardson, D. C. (2010). *Acta Cryst.* D**66**, 12–21.
Collyer, C., Henrick, K. & Blow, D. (1990). *J. Mol. Biol.* **212**, 211–235.
Corbett, M. C., Latimer, M. J., Poulos, T. L., Sevrioukova, I. F., Hodgson, K. O. & Hedman, B. (2007). *Acta Cryst.* D**63**, 951–960.
Emsley, P., Lohkamp, B., Scott, W. G. & Cowtan, K. (2010). *Acta Cryst.* D**66**, 486–501.
Evans, P. (2006). *Acta Cryst.* D**62**, 72–82.
Evans, P. R. (2011). *Acta Cryst.* D**67**, 282–292.
Evans, P. R. & Murshudov, G. N. (2013). *Acta Cryst.* D**69**, 1204–1214.
Fenn, T. D., Ringe, D. & Petsko, G. A. (2002). *1muw*, doi:10.2210/pdb1MUW/pdb.
Fenn, T. D., Ringe, D. & Petsko, G. A. (2004). *Biochemistry*, **43**, 6464–6474.
Garman, E. (1999). *Structure*, **7**, R291–R299.
Garman, E. F. (2010). *Acta Cryst.* D**66**, 339–351.
Garman, E. F. & Grime, G. W. (2005). *Prog. Biophys. Mol. Biol.* **89**, 173–205.
Gerstel, M., Deane, C. M. & Garman, E. F. (2015). *J. Synchrotron Rad.* **22**, 201–212.
Grabolle, M., Haumann, M., Müller, C., Liebisch, P. & Dau, H. (2006). *J. Biol. Chem.* **281**, 4580–4588.

Grime, G. (1996). *Nucl. Instrum. Methods Phys. Res. B*, **109–110**, 170–174.
Grime, G., Dawson, M., Marsh, M., McArthur, I. & Watt, F. (1991). *Nucl. Instrum. Methods Phys. Res. B*, **54**, 52–63.
Gutmanas, A., Alhroub, Y., Battle, G. M., Berrisford, J. M., Bochet, E., Conroy, M. J., Dana, J. M., Fernandez Montecelo, M. A., van Ginkel, G., Gore, S. P., Haslam, P., Hatherley, R., Hendrickx, P. M., Hirshberg, M., Lagerstedt, I., Mir, S., Mukhopadhyay, A., Oldfield, T. J., Patwardhan, A., Rinaldi, L., Sahni, G., Sanz-Garcia, E., Sen, S., Slowley, R. A., Velankar, S., Wainwright, M. E. & Kleywegt, G. J. (2014). *Nucleic Acids Res.* **42**, D285–D291.
Holton, J. M. (2009). *J. Synchrotron Rad.* **16**, 133–142.
Jenkins, J., Janin, J., Rey, F., Chiadmi, M., van Tilbeurgh, H., Lasters, I., De Maeyer, M., Van Belle, D., Wodak, S. J., Lauwereys, M., Stanssens, P., Mrabet, N. T., Snauwaert, J., Matthyssens, G. & Lambeir, A.-M. (1992). *Biochemistry*, **31**, 5449–5458.
Jokela, J., Pastinen, O. & Leisola, M. (2002). *Enzyme Microb. Technol.* **31**, 67–76.
Joosten, R. P., Long, F., Murshudov, G. N. & Perrakis, A. (2014). *IUCrJ*, **1**, 213–220.
Kabsch, W. (2010). *Acta Cryst.* D**66**, 125–132.
Kantardjieff, K. A. & Rupp, B. (2003). *Protein Sci.* **12**, 1865–1871.
Kmetko, J., Husseini, N. S., Naides, M., Kalinin, Y. & Thorne, R. E. (2006). *Acta Cryst.* D**62**, 1030–1038.
Kovalevsky, A. Y., Hanson, L., Fisher, S. Z., Mustyakimov, M., Mason, S. A., Trevor Forsyth, V., Blakeley, M. P., Keen, D. A., Wagner, T., Carrell, H., Katz, A. K., Glusker, J. P. & Langan, P. (2010). *Structure*, **18**, 688–699.
Kumar, K. S. D., Gurusaran, M., Satheesh, S. N., Radha, P., Pavithra, S., Thulaa Tharshan, K. P. S., Helliwell, J. R. & Sekar, K. (2015). *J. Appl. Cryst.* **48**, 939–942.
Langer, G., Cohen, S. X., Lamzin, V. S. & Perrakis, A. (2008). *Nat. Protoc.* **3**, 1171–1179.
Lavie, A., Allen, K. N., Petsko, G. A. & Ringe, D. (1994). *Biochemistry*, **33**, 5469–5480.
Lee, M., Rozeboom, H. J., de Waal, P. P., de Jong, R. M., Dudek, H. M. & Janssen, D. B. (2017). *Biochemistry*, **56**, 5991–6005.
Lübben, A. V. & Sheldrick, G. M. (2019). *J. Appl. Cryst.* **52**, 669–673.
Matthews, B. W. (1968). *J. Mol. Biol.* **33**, 491–497.
Maxwell, J., Campbell, J. & Teesdale, W. (1989). *Nucl. Instrum. Methods Phys. Res. B*, **43**, 218–230.
Meilleur, F., Snell, E. H., van der Woerd, M. J., Judge, R. A. & Myles, D. A. A. (2006). *Eur. Biophys. J.* **35**, 601–609.
Munshi, P., Snell, E. H., van der Woerd, M. J., Judge, R. A., Myles, D. A. A., Ren, Z. & Meilleur, F. (2014). *Acta Cryst.* D**70**, 414–420.
Murray, J. & Garman, E. (2002). *J. Synchrotron Rad.* **9**, 347–354.
Murray, J. W., Rudiño-Piñera, E., Owen, R. L., Grininger, M., Ravelli, R. B. G. & Garman, E. F. (2005). *J. Synchrotron Rad.* **12**, 268–275.
Murshudov, G. N., Skubák, P., Lebedev, A. A., Pannu, N. S., Steiner, R. A., Nicholls, R. A., Winn, M. D., Long, F. & Vagin, A. A. (2011). *Acta Cryst.* D**67**, 355–367.
Nave, C. (1995). *Radiat. Phys. Chem.* **45**, 483–490.
O'Neill, P., Stevens, D. L. & Garman, E. (2002). *J. Synchrotron Rad.* **9**, 329–332.
Owen, R. L., Rudiño-Piñera, E. & Garman, E. F. (2006). *Proc. Natl Acad. Sci. USA*, **103**, 4912–4917.
Pedersen, S. (1993). *Bioprocess Technol.* **16**, 185–208.
Perrakis, A., Morris, R. & Lamzin, V. S. (1999). *Nat. Struct. Biol.* **6**, 458–463.
Rangarajan, M., Asboth, B. & Hartley, B. S. (1992). *Biochem. J.* **285**, 889–898.
Ravelli, R. B. & McSweeney, S. M. (2000). *Structure*, **8**, 315–328.
Schray, K. J. & Mildvan, A. S. (1972). *J. Biol. Chem.* **247**, 2034–2037.
Sheldrick, G. M. (2015). *Acta Cryst.* C**71**, 3–8.
Shelley, K. L., Dixon, T. P. E., Brooks-Bartlett, J. C. & Garman, E. F. (2018). *J. Appl. Cryst.* **51**, 552–559.
Snell, E. H., van der Woerd, M. J., Damon, M., Judge, R. A., Myles, D. A. A. & Meilleur, F. (2006). *Eur. Biophys. J.* **35**, 621–632.
Ten Eyck, L. F. (1973). *Acta Cryst.* A**29**, 183–191.
Weik, M., Ravelli, R. B., Kryger, G., McSweeney, S., Raves, M. L., Harel, M., Gros, P., Silman, I., Kroon, J. & Sussman, J. L. (2000). *Proc. Natl Acad. Sci. USA*, **97**, 623–628.
Whitaker, R. D., Cho, Y., Cha, J., Carrell, H. L., Glusker, J. P., Karplus, P. A. & Batt, C. A. (1995). *J. Biol. Chem.* **270**, 22895–22906.
Whitlow, M., Howard, A. J., Finzel, B. C., Poulos, T. L., Winborne, E. & Gilliland, G. L. (1991). *Proteins*, **9**, 153–173.
Williams, R. J. (1985). *FEBS J.* **150**, 231–248.
Winn, M. D., Ballard, C. C., Cowtan, K. D., Dodson, E. J., Emsley, P., Evans, P. R., Keegan, R. M., Krissinel, E. B., Leslie, A. G. W., McCoy, A., McNicholas, S. J., Murshudov, G. N., Pannu, N. S., Potterton, E. A., Powell, H. R., Read, R. J., Vagin, A. & Wilson, K. S. (2011). *Acta Cryst.* D**67**, 235–242.
Zeldin, O. B., Brockhauser, S., Bremridge, J., Holton, J. M. & Garman, E. F. (2013*a*). *Proc. Natl Acad. Sci. USA*, **110**, 20551–20556.
Zeldin, O. B., Gerstel, M. & Garman, E. F. (2013*b*). *J. Appl. Cryst.* **46**, 1225–1230.
Zheng, H., Chruszcz, M., Lasota, P., Lebioda, L. & Minor, W. (2008). *J. Inorg. Biochem.* **102**, 1765–1776.